Unique Properties of Thermally Tailored Copper: Magnetically Active Regions and Anomalous X-ray Fluorescence Emissions

Christopher J. Nagel* and Dudley R. Herschbach*

Continuum Energy Technologies, LLC, 421 Currant Road, Fall River, Massachusetts 02720

Received: August 27, 2009; Revised Manuscript Received: October 20, 2009

When high-purity copper ($\geq$99.98%$_{wt}$) is melted, held in its liquid state for a few hours with iterative thermal cycling, then allowed to resolidify, the ingot surface is found to have many small regions that are magnetically active. X-ray fluorescence analysis of these regions exhibit remarkably intense lines from "sensitized elements" (SE), including in part or fully the contiguous series V, Cr, Mn, Fe, and Co. The XRF emissions from SE are far more intense than expected from known impurity levels. Comparison with blanks and standards show that the thermal "tailoring" also introduces strongly enhanced SE emissions in samples taken from the interior of the copper ingots. For some magnetic regions, the location as well as the SE emissions, although persistent, vary irregularly with time. Also, for some regions extraordinarily intense "sensitized iron" (SFe) emissions occur, accompanied by drastic attenuation of Cu emissions.

Introduction

In previous work, extending over several years, we found that X-ray fluorescence analysis (XRF) of high-purity copper ($\geq$99.98%$_{wt}$) subjected to "hot metal tailoring" typically indicates appreciable amounts (up to 1%$_{wt}$) of "sensitized elements" (SEs), including Na, S, Al, Cl, K, and Ca, not present at such significant levels in the untailored material.[1,2] The tailoring appears to markedly enhance the intensity of XRF emissions, thereby making minor impurities seem far larger. The tailoring also induces substantial changes in properties such as melting point, hardness, color, resistivity, Hall effect, specific heat, dc magnetization, and ac susceptibility, examined over a wide temperature range. The induced changes differ for three versions of the thermal tailoring protocol. These have in common adding small amounts of graphite to molten Cu, cycling the melt over temperature ranges extending below and above carbon saturation, flushing the melt with inert gases (N_2, He, Ne, Ar, Kr), and cooling to solidify. The protocols differ in cycle and overall durations, gas mixture compositions and flow rates, and use or not of irradiating light sources. Although some of the property changes induced by tailoring resemble those familiar for impure copper, some features differ markedly. Moreover, over a span of time ranging from minutes to years some SE concentrations in a given sample were found to decay by factors varying from 2 to 10. Fluctuations in associated physical properties (e.g., magnetism) were also observed.

The evidence that tailoring does introduce SEs and change properties is now extensive, but how this comes about is not understood. Recently, we have obtained much superior XRF instrumentation which has enabled more incisive analysis. This paper reports results obtained thereby for copper treated by a more rudimentary version of tailoring, which sufficed to produce in the ingot surface many small regions that are magnetically active. We find the XRF spectra of these regions exhibit novel features, including a contiguous series of SEs extending from V, Cr, Mn, Fe, to Co. Auxiliary tests show this series cannot be attributed to Bragg peaks or mere aggregation of impurities. Among the novel properties are time-dependence of the positions and SE content of the magnetic regions and correlations between increases in fluorescence from SEs with decreases in the fluorescence from copper. These observations provide more compelling evidence for SEs but how tailoring introduces such sensitization effects awaits theoretical explanation.

* To whom correspondence should be addressed. E-mail: nagel_cj@yahoo.com (C.J.N.); herschbach@chemistry.harvard.edu (D.R.H.).

Experimental Procedures

Material Tailoring: General. We first outline our previous tailoring protocols,[1,2] which also produced copper ingots with magnetically active regions, in order to place in context the simplified version employed in the work reported in this paper. Figure 1 provides a flowchart, displaying operations involved in three versions of tailoring. In each, copper was heated to its melting point and above using an induction furnace lined with a high-purity ($\geq$99.68%$_{wt}$) alumina crucible. Small amounts of high-purity graphite ($\geq$99.9995%$_{wt}$) were added via a lance. The molten metal was then sequentially subjected to temperature sweeps (T-sweeps), designed to vary the carbon concentration in a periodic manner, typically sinusoidal, to create subsaturated ("under") and supersaturated ("over") solutions. Typically, the initial T-sweeps are subsaturation, after which the melt is held at equilibrium corresponding to carbon saturation for a specified time ("hold"), and further sweeps then made under supersaturated conditions. Finally, cooling to solidification occurs via a specified time and temperature profile.

The protocols differ in sub-events imposed during the warm-up, T-sweeps, hold, and cooling stages; the variants involve injecting inert gases, often mixtures, or varying the direct current (via voltage), power, or frequency supplied to the material within the crucible enclosed by the induction furnace.

Material Tailoring: Simplest Version. In most of the experiments reported here, no graphite was added to the copper, and gas injections, as well as current, power, or frequency variations were likewise not used. The reactor was a 100-lb induction furnace (Inductotherm), fitted with a 73-30R Power-trak power supply with an attached induction coil (38.1 cm o.d. $\times$ 33 cm i.d. $\times$ 43.2 cm tall). The active zone of the coil comprised 8 active wraps (total height 31.1 cm). There is a single inactive cooling wrap above (by 5.7 cm) the top active

10.1021/jp908299q CCC: $40.75
Published on Web 11/19/2009

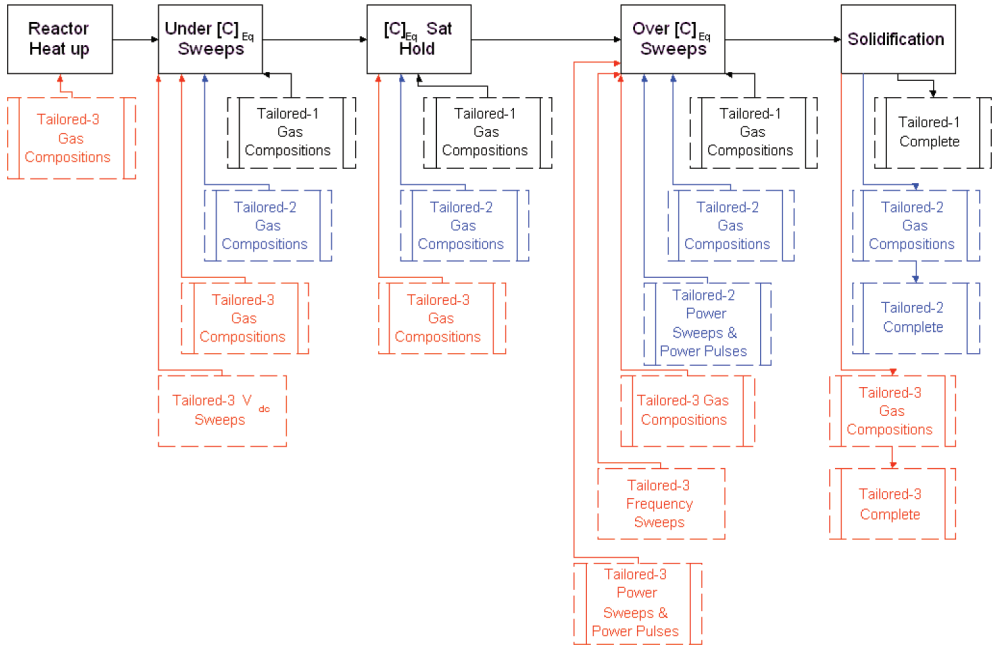

Figure 1. Flowchart for tailoring procedures. Reference 2 provides a detailed description.

wrap and another inactive cooling wrap below (by 6.0 cm) the bottom active wrap. The furnace had a high-purity ($\geq$99.99%$_{wt}$) graphite cap and a ceramic liner, a cylindrical alumina-based crucible (99.68%$_{wt}$ Al_2O_3, 0.07%$_{wt}$ SiO_2, 0.08%$_{wt}$ Fe_20_3, 0.04%$_{wt}$ CaO, 0.12%$_{wt}$ Na_20; 4.5 in. o.d. $\times$ 3.75 in. i.d. $\times$ 14.5 in. depth).

In a run, the reactor was loaded with 9080 g of copper ($\geq$99.98%$_{wt}$) through its charging port. A slight positive pressure (at $\sim$3.45 kPa) of high-purity Ar ($\geq$99.9997%$_{vol}$) was maintained in the reactor using a continuous backspace purge. The induction furnace was programmed to heat the crucible to 1623 K over a 16.5 h interval, at a rate no greater than 83 °C/h, as limited by the integrity of the crucible. The furnace operated at a frequency (in the range 0 $-$3000 Hz) determined by a temperature controlled feedback loop governed by a control unit (Omega Model CN300). After the 16.5 h heat up, a 3 h hold was programmed. For the runs used in this work (designated 14-02-05 and 14-08-04, a replicate), the programmed crucible temperature (1623 K) was not attained, even after applying full power (40 kW) for 3 h. The resultant power ramp up imposed via the induction furnace control loop resulted in asymmetric thermal cycling of the material similar to the thermal sweeps used in the usual tailoring.[3] The final temperature achieved in runs 14-02-05 and 14-08-04 was 1503 and 1578 K, respectively.

Sample Preparation. All sample cleaning and preparation conformed to industry-established standards. Depending on the nature of the surface, some materials are flycut (flatness defined by a maximum elevation change of $\sim$10 μm) and then cleaned with isopropyl alcohol. For XRF and some other analytical methods, samples were prepared by cutting a cube shape ($\sim$3.0 cm) from the center of the cooled ingot. An axial and a radial edge are then denoted according to the cylindrical geometry of the crucible. To provide a smooth surface for analysis, the axial and radial faces are either flycut according the NIST XRF standards or in rare cases, sequentially polished to obtain an even flatter surface. In the latter case, the sample faces are sequentially polished first with 80, 120, and 340 alumina grit polishing compounds, then followed by 400 and 600 silica polishing compounds, and finished with a 15 μm diamond paste. In all cases, the sample is cleaned after surface preparation with isopropyl alcohol and then placed in a cassette/holder. Sample handling is performed using clean gloves and integrity is maintained in sample cassette history for subsequent experiments. These experimental protocols have been experimentally and statistically validated to maintain an appropriate level of cleanliness.

XRF Instrumentation. Our previous work[1,2] used an ARL 8410 XRF instrument to analyze the elemental composition of the sample ingots. This is a sequential wavelength dispersive spectrometer (WDS). The ARL uses a standardless Uniquant algorithm to detect and quantify the presence of various elements, chiefly based on the K_α line of each element, although secondary and tertiary lines are used as necessary. The ARL detects elements from Na to U, with a lower detection limit of about 20 ppm. This instrument is widely used for routine analysis due to its excellent energy resolution ($\leq$1 eV), but its poor spatial resolution, defined by a 29 mm elliptical mask, and lack of scanning capability limited its value for our work.

Most spectra reported in this paper were obtained using a portable micro-X-ray fluorescence energy dispersive spectrometer (Bruker AXS ARTAX), mounted on a mobile head capable of scanning along x and y axes. The measuring head can be positioned by a control unit using step motors. This enables automatic measuring cycles at a single point or along a specified line or over an area of 45 $\times$ 45 mm^2. The fluorescence excited by a collimated or focused X-ray beam is monitored by a cooled semiconductor detector, which converts the emission into current pulses that are amplified and digitized in a preamplifier and an X-ray digital signal processor, XSPV. The XSPV is the primary processor for measurement, control, regulation, and communication. A spectroscopic signal amplifier and processor (XDSP) transfers the digital signal to a computer which stores the data. The pulse trains from the detector are displayed as an intensity/energy spectrum. The computer also evaluates the relative elemental composition of the sample, taking account of the excitation energy, detector calibration, and spectral intensity distribution of the fluorescence lines.

The ARTAX instrument employs alternate excitation X-ray tubes (W, Cr, and Mo); these provide means to more precisely characterize spectral regions of interest and eliminate false readings that otherwise can arise from the detector picking up

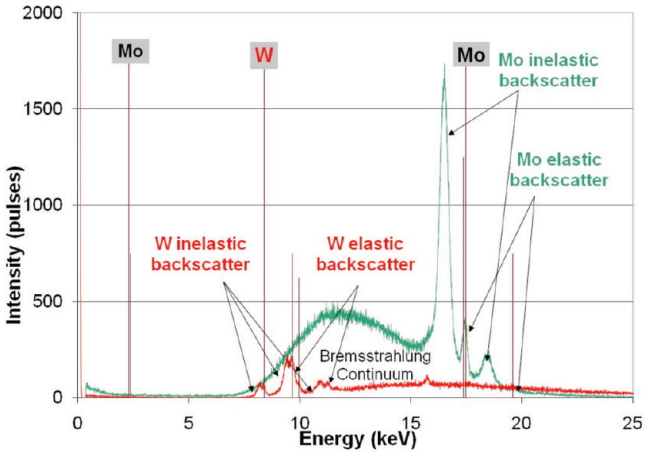

Figure 2. ARTAX ED-XRF excitation spectra taken with a polyethylene base in air with a 0° angle of incidence. Mo tube (green) used a 60μm polycapillary lens (70 μm average observation region), 40 kV, 700 μA, 120 s. scans. W tube (red) used a 650 μm collimator, 40 kV, 1000 μA, 120 s scans.

radiation from the excitation element. Filters made of metal foils (e.g., Al, Ni, Mo, Zr, etc.) are used to absorb X-rays coming from the X-ray tube to eliminate those energies from the backscattered radiation from the sample. The filters, mounted on a slide which permits easy exchange and precise positioning, are matched to the interactions of interest.

Analytical Protocols. When using the ARL, care is taken to ensure the sample is tight fit in the holder to maintain reproducibility of the scanning surface. The sample in the holder is loaded into the instrument and spun. The orientation of the detector crystal with respect to the sample and the photon detector is controlled synchronously such that characteristic X-ray lines can be measured. A sequential measurement consists of positioning the diffraction crystal at a given angle θ and the detector at 2θ and counting for a given period of time. The crystal and detector are then rotated to a different angle for the next characteristic X-ray line. Uniquant Version 2 software (Omega Data Systems) controls the crystal and detector placement and reduces the data to a list of elemental composition with the associated concentrations.

The ARTAX instrument is much more versatile by virtue of its ability to scan continuously small spatial locations on the samples and the energy of fluorescence photons.[4] Samples are placed flat under the ARTAX head and then the area scanned. The ARTAX unit has a method for focusing to allow for optimum detection by setting the proper distance between the sample and the X-ray tube/detector. This also means that all readings are taken with the same geometry, resulting in more consistent results from sample to sample.

Samples can be analyzed by measuring a single point, a line of points, or an area of points. For all three modes, the measurement procedure is identical. The ARTAX head moves to the correct position and waits a predetermined time for head stabilization, then detects the X-ray emissions coming from the sample for a preset interval. This process is repeated until the desired scan is completed. Energy calibration is validated pre- and postanalysis to ensure consistent results. The operator can set the desired spacing between points and the amount of time that the unit records X-ray emissions at each point. The X-ray spectra can be viewed in real time and output into Microsoft Excel.

Figure 2 shows the excitation spectra as generated by the ARTAX ED-XRF using a tungsten (W) tube (shown in red) and a molybdenum (Mo) tube (shown in green), both with a 315 μm Al filter directed at a polyethylene target in air. For the region most pertinent to our experiments, 5−9 keV, the background is extremely low. All X-rays below ~8 keV were filtered by the 315 μm Al filter.

Results and Discussion

Figure 3 illustrates typical evidence for "sensitized elements" as observed in our previous work using the ARL instrument.[2] XRF results for copper, after treatment by the tailoring protocols of Figure 1, are compared with those for an untreated sample. The lower detection limit (LDL) is about 20 ppm (0.002%$_{wt}$). The concentrations indicated for most impurities in the untreated copper are below or not much above the LDL. In contrast, for the tailored samples, several elements, among them Na, Al, S, Cl, Mn, and Fe, appear to be present at levels 1 or 2 orders of magnitude above those in the untreated copper. For both the tailored and untailored cases, the samples were cut from the interior of ingots (as specified above) to ensure that the striking differences seen in the tailored samples do not arise from concentration of impurities near the ingot surface.

Both the tailored samples and the untreated copper were also analyzed by high-resolution glow discharge mass spectrometry (GD-MS). This found contaminant levels consistent with the untreated copper and, for the tailored samples (14-00-01, subsequently referenced as Ingot A), much lower than indicated by the ARL WD-XRF results (Figure 4). GD-MS measures bulk composition whereas ARL WD-XRF probes only to modest depths (e.g., ~60 μm in high-purity copper). Thus, there was concern that tailoring might foster concentration of impurities near the surface or otherwise somehow amplify their apparent concentrations as measured by ARL WD-XRF. Therefore, as in Figure 3, all data for Figure 4 were obtained from samples cut from the interior of ingots. As a test, the untailored ("natural") copper was melted and held in the same system reactor (high alumina crucible liner) in order to have a "blank" that should have been subjected to the same potential sources of contamination and contaminant distribution profile as the tailored materials. Ten ARL analyses of this blank (14-08-01) were performed and averaged. The results were consistent with the GD-MS, as well as the known impurities in the natural copper, but as seen in Figures 3 and 4, indeed indicated concentrations well below what XRF finds in the tailored samples.

Magnetically Active Regions. In this paper, we shall consider almost solely properties of magnetically active regions ("spots") introduced by tailoring copper. Figure 5 displays a striking example, in which such spots appear as discrete, roughly evenly spaced points, along an approximately sinusoidal curve. The spots (typically 2.5 mm dia) are not visible to the eye or on microscopic examination but are found, at room temperature, to exhibit equivalent attraction to both poles of a 1/8 in. Nd/Fe/B magnet. Some spots attract iron filings; others do not. Also, a few spots show an appreciable but partial Meissner effect, tilting the probe magnet disk by 35−45°. Gauss meter measurements give an essentially zero reading for all spots, however. On cooling the ingot via liquid nitrogen (to ~77 K), the attraction for filings and the partial Meissner effect increases for some spots and weakens for others, but these variations do not exhibit a regular pattern. A further curious property is the metastable character of the spots: both their attractive strength and location on the surface of the ingot change with time. For instance, over 8 years, several seemingly typical spots were observed to either disappear completely and then reappear at a later time or to migrate away from their original positions by

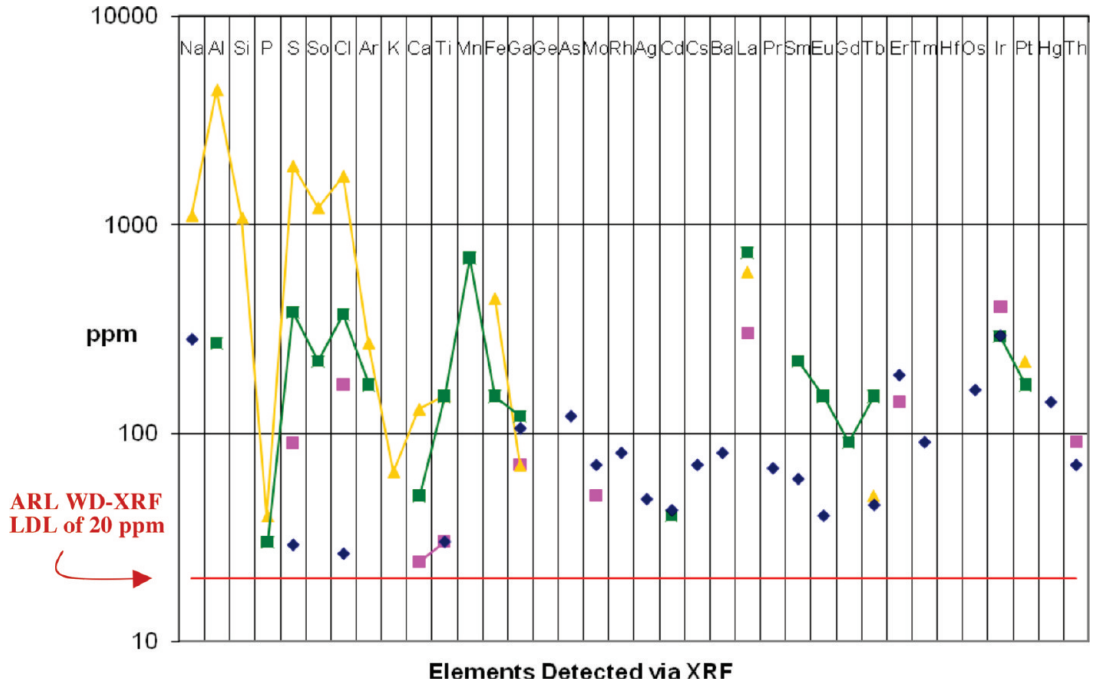

Figure 3. Evidence for "sensitized elements, " from comparison of ARL WD-XRF elemental analysis results for copper tailored by variations of the three protocols shown in Figure 1. Symbols denote data for protocols 1, ■; 2, ▲; 3, ●; obtained in runs designated 03-99-013; 03-99-021a; 03-99-021b, respectively. A nondetect is not reported in the graph. A "blank" untailored sample (◆) designated 14-08-01 is also plotted. The latter "blank" sample was held at temperatures comparable to the tailored runs for 3 days in the standard high alumina crucible. Reported concentrations are the average of all detections above the lower detection limit (20 ppm) obtained from 10 different ARL WD-XRF analyses of the same sample.

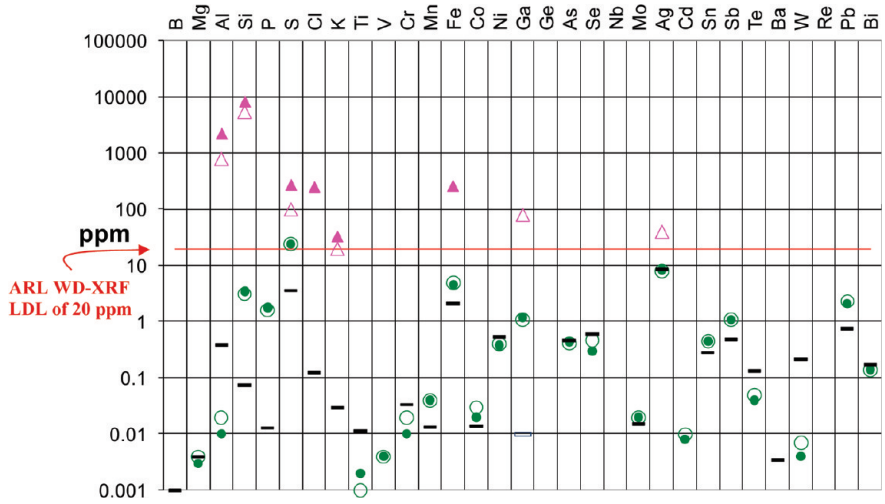

Figure 4. Comparison of WD ARL XRF elemental analysis and GD-MS elemental analysis results for tailored copper showing significantly different results. Symbols denote data for GD-MS analysis of 14-00-01 (axial, ●) and (radial, ○); XRF analysis of 14-00-01 (axial, ▲) and (radial, Δ); and (−) denotes the average composition of the untailored starting material as determined by GD-MS. For Ga, the average was taken to be the LDL as none was detected in the starting material. By comparison to other melted systems, Ga in 14-08-01 of Figure 3, was identified as 0.14 ppm. Protocol 1 of Figure 1 was used to prepare 14-00-01.

distances of 2−5 mm in most cases and in others by distances exceeding 1 cm.

Figure 5 displays "unrolled" 360° maps, made in 2000 and 2008, of the spots showing magnetic attraction on the surface of the ingot pictured in Figure 5. Over this 8-year span, the total number of spots remained about 50. Some spots appeared to stay in place (moved less than 1 mm); there were about six such spots (in overlay enclosed in red boxes: two between 225−240°, two at 255°, one near 275°, and one near 115°). About 14 other spots remained very close (within 3 mm); the displacements did not exhibit any systematic shift. A cluster of points seen in 2000 (purple oval, near 345°) had by 2008 disappeared, while three new clusters appeared (orange ovals, near 30°, 45°, and 150°). The roughly sinusoidal distribution observed in 2000 (cf. Figure 5) had become less evident in 2008, although some patterning persists (e.g., series of spots between 15° and 45° and between 75° and 105°, both marked with blue arrows).

In view of the potential for contaminants in the system to aggregate at the surface (cf. Appendix B) or accumulate at grain boundaries during cooling, we carried out an ARTAX ED-XRF elemental analysis across multiple grain boundaries on the ingot surface at four randomly chosen locations. Each of these line scans consisted of 26 sequential measurements taken in series

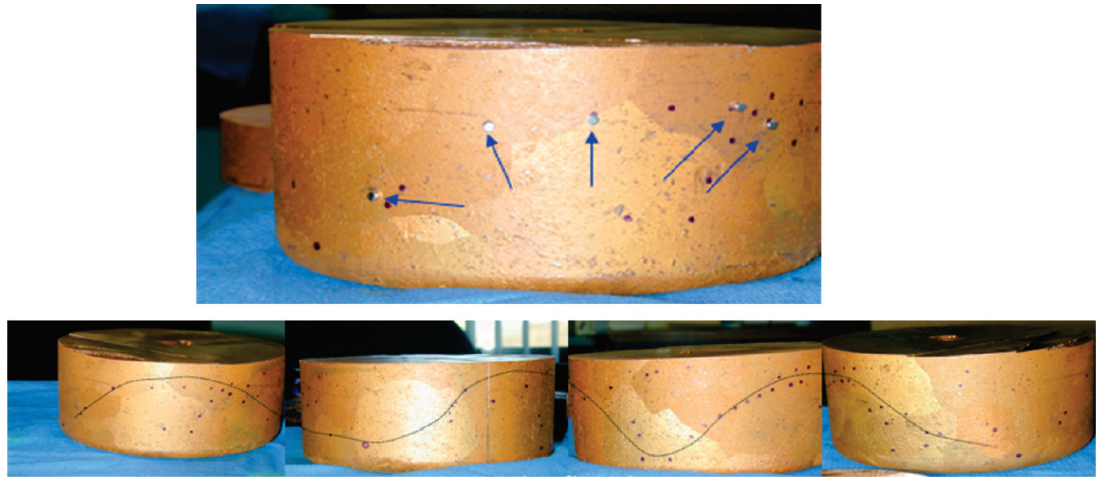

Figure 5. Distribution of magnetically active "spots" that appeared in tailored copper (run 14-00-01, using protocol designated tailored-1 in Figure 1). 360° view shown. In close-up view, arrows point to five spots that are holding 1/8 in. diameter Nd/B/Fe magnets. The four views shown in series correspond to successive 90° rotations of the ingot. The diameter of the ingot is ~7.5 in.

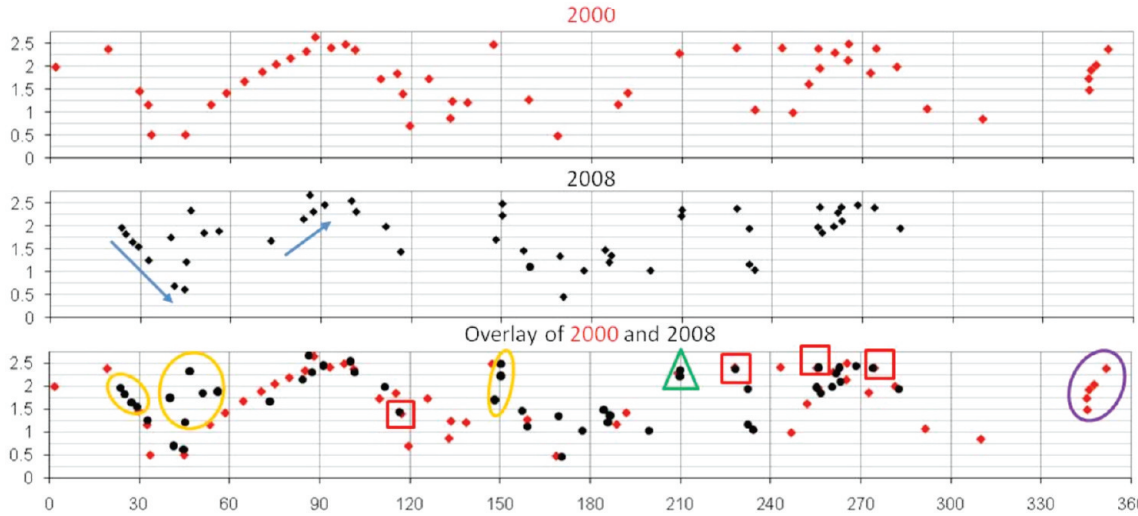

Figure 6. Spots of magnetic attraction are displayed for tailored copper ingot 14-00-01 (see Figure 5) for the years 2000 and 2008. Bottom panel shows an overlay. Red dots denote 2000 data, black dots denote 2008 data. Some spots (enclosed in red boxes) appear identical (i.e., moved less than 1 mm). Some clustered spots seen in 2000 (purple oval) had disappeared by 2008, while three new clusters appeared (orange ovals). One spot (in green triangle) appeared to split into two. The grid height is 2.625 in., and the grid length is 23.25 in.

with 50% overlap spanning the clearly visible grain boundaries. No signs of agglomeration or accumulation of known ferromagnetic contaminants was found to occur along or within the grain boundaries.

We also tested for contamination effects by deliberately adding ~3 g of Fe to a molten Cu sample (~7 kg), thereby introducing Fe at a level (~400 ppm) comparable to the nominal levels of sensitized Fe seen in tailored ingots (cf. Figures 3 and 4). The melt was then allowed to solidify without undergoing a tailoring protocol. Samples cut from either the surface or the interior of the resulting ingot did not exhibit magnetic spots or enhanced intensity or variation with time of XRF emissions.

Until obtaining the state-of-the-art ARTAX instrumentation, we were unable to examine closely, with high spatial resolution, the magnetic spots by means of XRF spectroscopy. We now report results of ARTAX analysis that exemplify a variety of properties of such spots. Some appear on the ingot pictured in Figure 5 (designated, for brevity, as "Ingot A"), others on another ingot tailored by the same protocol ("Ingot B"). Also, we report XRF spectra and magnetically active regions in copper treated by our "simplest version" of tailoring (Ingots C and D). Indeed, that simplest protocol produces a higher density of magnetic spots with a richer content of sensitized elements.

XRF Spectra of Ingots A and B. For the A ingot (14-00-01), we carried out an XRF analysis of two spots: one, denoted A1, attracted both our Nd/Fe/B probe magnet and Fe filings; the other, denoted A2, attracted the probe magnet more strongly but did not attract Fe filings. These were compared with a nearby "null" point on the ingot that did not have a magnetic response. The XRF spectra showed the nominal concentration of iron in both A1 and A2 was much higher than the null point, but with a dramatic time variation, as seen in Figure 7. Initially, the Fe K_α line (actually a superposition of lines denoted $K_{\alpha 1}$ and $K_{\alpha 2}$) was about twice as strong for spot A2 as A1; 22 h later, this ratio was reversed and ~250 h later the ratio had become unity.

The odd changes with time led us to perform a remelt experiment to ascertain the behavior of the magnetism. An ingot designated A′ (14-08-10) was tailored via the simplest protocol and found to have magnetic spots, with density comparable to the A ingot. The A′ ingot was remelted and subjected to the same tailoring protocol. After solidification, magnetic spots reappeared, with similar density.

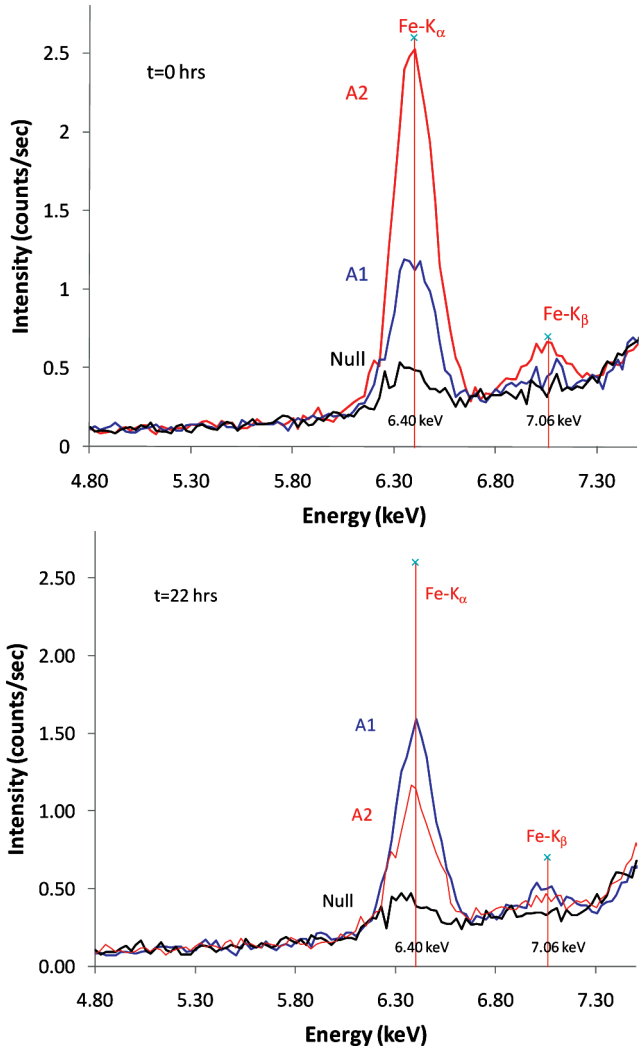

Figure 7. XRF spectra of A ingot (14-00-01) in the region of Fe K_α and K_β lines. Note, a Si escape peak is visible at 6.3 keV in the uncorrected null spectra shown.

For the B ingot (14-00-03), the high spatial resolution of the ARTAX instrument made it feasible to survey the Fe K_α and K_β lines at four points within each of two closely neighboring magnetic spots, denoted B1 and B2. The ratio K_α/K_β for a given atom is determined by relative transition probabilities. In actual environments, the ratio can be affected (~20%) by the X-ray excitation process (e.g., X-ray tube voltage and exciting X-ray beam filter), self-absorption within the sample, wavelength-dependent response, and efficiency of the crystal and detector. Also, accurate fitting of line shapes is important and difficult. Theoretical K_α/K_β values of 7.91 and 7.25, respectively, were obtained from relativistic Hartree−Fock calculations.[5] Experimental values of the K_α/K_β ratios for pure elemental Fe and Cu were found by Han, et al. to be 5.62 and 6.91, respectively.[6] Fe K_α/K_β ranges between 5.6 and 6.3 for a variety of XRF reference systems with variable excitation sources and detector types.[7] We confirmed agreement with those ratios for systems comparable to our systems, e.g., Fe seeded in high-purity copper and the high-purity copper NIST standards C1122 and C1251a. Variations in the measured K_α/K_β ratio are found to be very small (<2%) when using a given well-designed apparatus and technique.[7] For the tailored ingot, we found the scans of B1 and B2 magnetic spots gave K_α/K_β ratios that deviate more than 50% from the established range. Furthermore, in scanning a third spot some distance from B1 and B2, we observed a prominent Fe K_α line but the K_β was undetectable, although the background was very low where it should have appeared.

XRF analysis has been used in myriad studies of impurities in metals, but there seems to be no precedent for the anomalous time dependence and discrepant Fe K_α/K_β ratios that we observe for these magnetic spots.

XRF Spectra of Ingots C and D. For the C ingot (14-02-05), produced with the simplest version of tailoring, we show in Figure 8a four spectra obtained by using the ARTAX with a tungsten excitation tube and a 315 μm Al filter to scan a magnetically active surface region. The measurements were taken on a predesignated grid pattern shown in Figure 8b.

At each grid point, a 40 s reading was taken with ~50% overlap between points, thus comprising 22 × 16 measurements. The grid points are designated, starting in the lower left corner and proceeding across rows, then upward, such that the last measurement (no. 352) corresponds to the upper right corner. Upon locating regions of interest, ARTAX can be requested to plot a full energy spectrum. The four spectra of Figure 8 were compiled from measurements no. 271−274, which correspond to a horizontal progression along the grid through the magnetic spot. The spectra are plotted in three panels with different ranges of signal pulse intensities, as indicated.

These data exemplify the particularly strong evidence for sensitized elements found for ingots produced using the simplest tailoring protocol. The XRF signal pulse rates for Fe are remarkably high, 16% as large as for Cu. Those for V, Cr, Mn, and Co are much smaller, yet also much higher than expected from impurities in the copper. Other elemental detection techniques, such as GD-MS (Shiva Technologies, a unit of EAG, LLC, Syracuse, NY), analyzing bulk samples rather than a magnetic spot, indicate typically Fe, ~3 ppm; V, Cr, Mn, and Co, <0.05 ppm. These concentrations are much below the lower detection limits for ARTAX analysis of these elements. For copper alloys the lower detection limits can be matrix dependent, but typically LDLs for Fe ~70 ppm, for Mn >40 ppm, for Co ~10 ppm, and for Ni ~60 ppm can be achieved with a properly calibrated quantification routine using known standards of similar composition. However, for normal ARTAX operating conditions, the LDLs are much higher. Using the same conditions employed to obtain the spectra of Figure 8 (and others in this paper), we found that the ARTAX did not detect Fe in a NIST standard (C1251) that contained 285 ppm Fe. These observations reinforce many others we have made that for SEs tailoring greatly enhances XRF emission intensities.

Another exceptional aspect is the large variation of the intensity of the Cu K_α peak at different points of the grid, despite the great preponderance of copper over Fe and the other SEs. Decreases in the Cu intensity appear to be correlated, with increases in the intensity of the Fe K_α peak (and less clearly the other SEs). Figure 9 exhibits this relationship. Similar plots made using only the counts for each individual SE are also fairly linear, but with modestly different slopes.

Figure 10 contrasts the striking inverse coordination of the XRF emissions from Cu and Fe in the tailored C Ingot with the totally smooth and indifferent behavior obtained for a NIST beryllium−copper standard sample (SRM C1122). It contains ~97.4% copper and less than ~0.16% iron but much more Fe than the 99.98% copper used as our starting material. Thus, the results for the standard indicate what might be expected from a nontailored ingot, even one with far more iron than our ingots have. The very steady results exhibited by this standard are indeed usual with the ARTAX instrument (electronic stability $< \pm 1\%$) when applied to a flat material (surface fluctuation

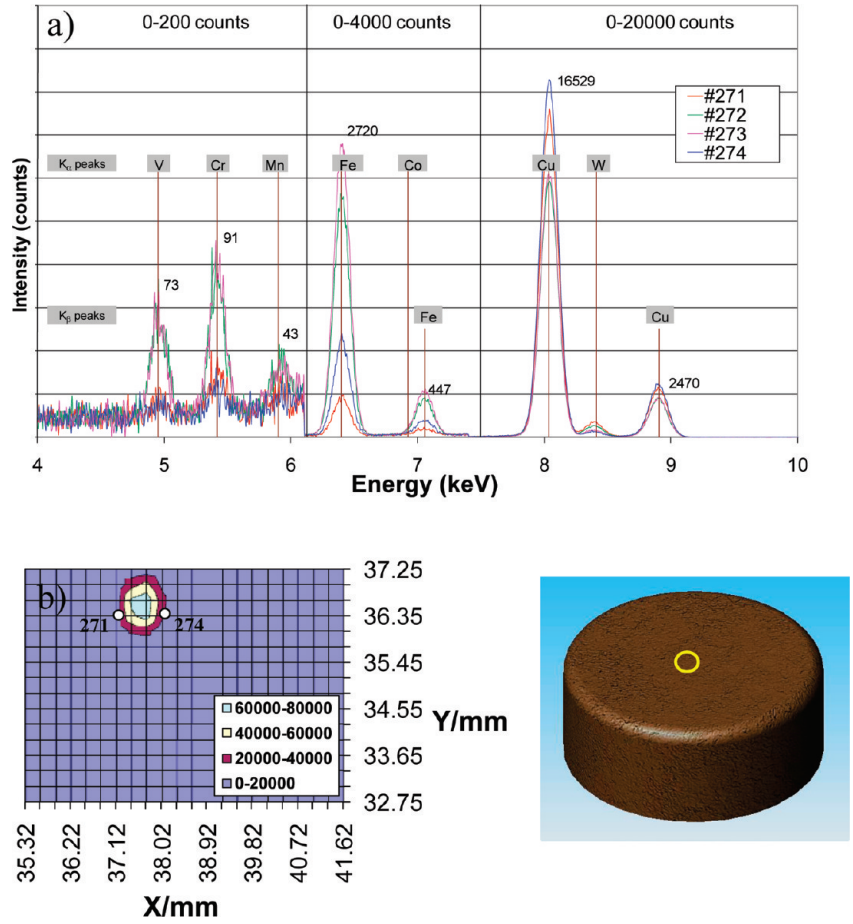

Figure 8. (a) XRF spectra for copper ingot C (14-02-05) for a magnetically active spot located (as pictured at upper center, yellow circle) in the approximate middle of the ingot bottom. (b) Plot showing Fe K_α signal pulses detected across the grid pattern employed in the spectral scans. White dots mark start (no. 271) and end (no. 274) of grid positions of four spectra scans. The spectra shown here (and in subsequent figures) have been corrected for background drift and Si escape peaks (at 6.3 keV) using algorithms provided by Bruker AXS. Analyses performed using ARTAX ED-XRF parameters: W tube, 650 μm collimator, 40 kV, 1000 μA, 315 μm Al Filter, 40 s/point scans.

$< \pm 10$ μm). Such a large modulation of the Cu XRF intensity as seen in Figures 9 and 10 is unprecedented.[8] We therefore obtained further spectra and considered other potential explanations.

Figure 11 shows five XRF spectra from another magnetic spot on ingot C. The sample preparation and ARTAX analysis were conducted in the same way as for Figure 8 and the scanning grid is similar. The emission peaks correspond to the K_α transitions for V, Cr, Mn, Fe, and Co, contiguous elements in the periodic table. Here we use a normalization scheme that adjusts the ordinate scale for each XRF feature to the highest signal pulse level it attains in scanning the five spectra. This brings out the remarkably parallel variation of the Cu K_α and K_β intensities and the opposite variation of that for the emissions from Fe and its contiguous SEs. In ordinary displays of spectra, using linear ordinate scales, such relationships are much harder to discern. These results nicely reinforce those of Figures 8−11.

We also examined ingot D (14-08-04), which likewise was produced by the simplest tailoring protocol. Figure 12 shows XRF spectra obtained from six distinct grid points within a rather large magnetically active region. Again, emissions corresponding to the contiguous series V through Co are seen; in this case, however, the Cr K_α is more prominent than that for Fe and Co appears distinctly.

A broader XRF census of the magnetic spots, on ingots C and D, as well as those subjected to other tailoring procedures, finds wide variation in the elemental composition. Some spots appear to contain only Fe; others just Fe + Co or Fe + Cr. The progression of several contiguous elements seen in Figures 8, 11, and especially 12 is unusual but not unique. In XRF spectra, such a regular progression of emission peaks arouses suspicion because Bragg scattering is a familiar source of extraneous emission peaks that arise from the crystal structure. However, diagnostic tests for Bragg scattering are readily made. X-ray diffraction studies performed by the Evans Analytical Group (Austin, TX) on samples cut from ingots C and D showed these have polycrystalline character with a strongly preferred orientation. Accordingly, as described in Appendix A, we carried out three standard tests for the presence of Bragg scattering. These conclusively ruled it out as a significant factor in our experiments.

Also questionable is the remarkable attenuation of 10−40% in the characteristic XRF emission of the Cu K_α and K_β lines (as exhibited in Figure 8−12), correlated with increase in emissions from SFe and contiguous SEs. The suspicion is that agglomeration of impurity Fe into the magnetic spots, due to azeotropic cooling occurring in tailoring, might filter the Cu emissions, thus introducing an inverse correlation with the local Fe concentration. As a further experimental test, we repeated the XRF analysis of the magnetic spot examined in Figure 11, using the Mo tube rather than the W tube and thereby improving the spatial resolution 10-fold, to about 70 μm. As seen in Figure 13, the results are similar to those obtained with the W tube, but even larger attenuations of the Cu K_α and K_β emissions were observed, up to about 90%, with a concomitant growth in the SFe emissions. Figure 14 compares the variation in pulse

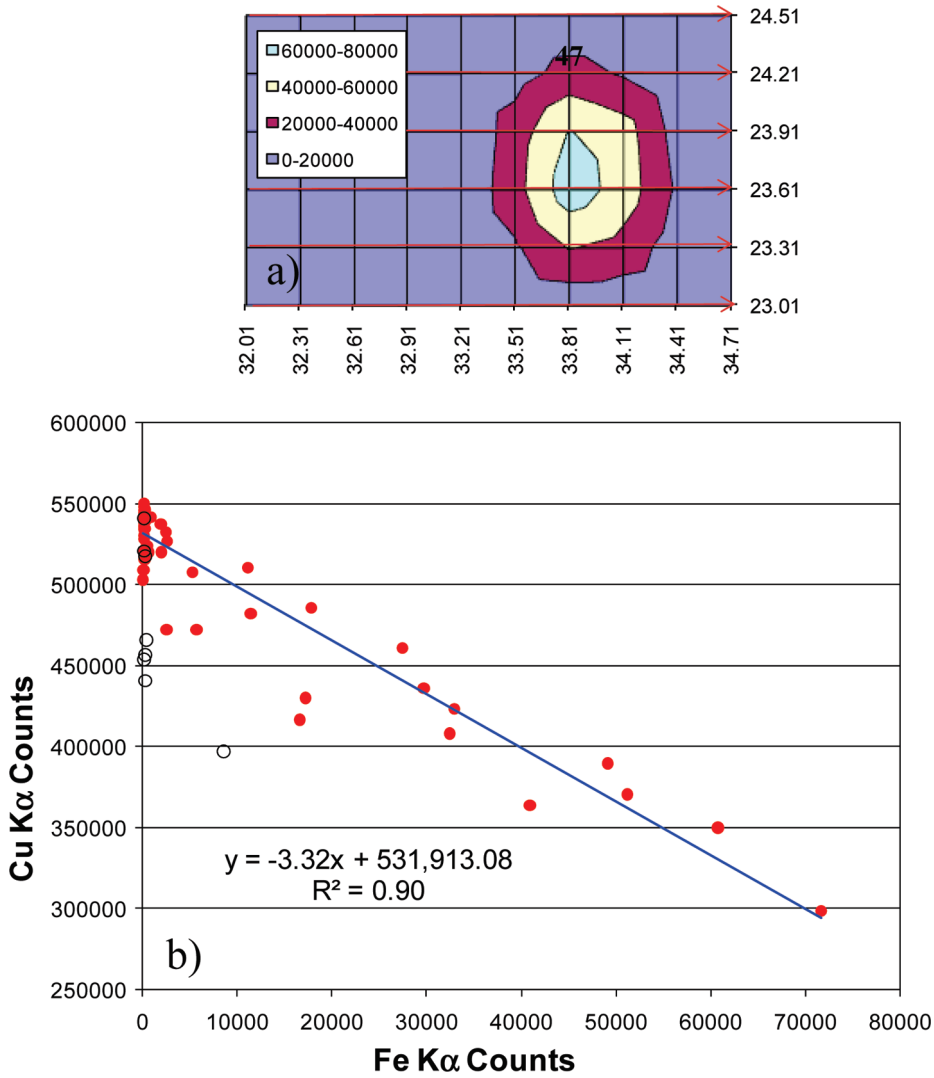

Figure 9. (a) Profile map showing plot of Fe K_α intensity over the ED-XRF scan grid for a magnetic spot region on Ingot C (14-02-05); the location of the spot is near the edge of the bottom of the ingot (within yellow circle in Figure 11, upper right). Arrows indicate direction in which the ARTAX head moves in scanning, left to right, bottom to top. (b) Plot showing approximately linear correlation between decrease in XRF photon counts for Cu K_α emissions and increase in Fe K_α emissions. The correlation coefficient is $R^2 = 0.90$. The data points are from scans made at each of the 60 vertices of the scanning grid. For eight points (denoted by open circles, ○) large Zr emissions (>1000 counts) were observed. These points were not included in evaluating R^2. Since Zr is present in the reactor containment system (in insulation above the lid of the crucible), its appearance indicates contamination by a speck of refractory material.

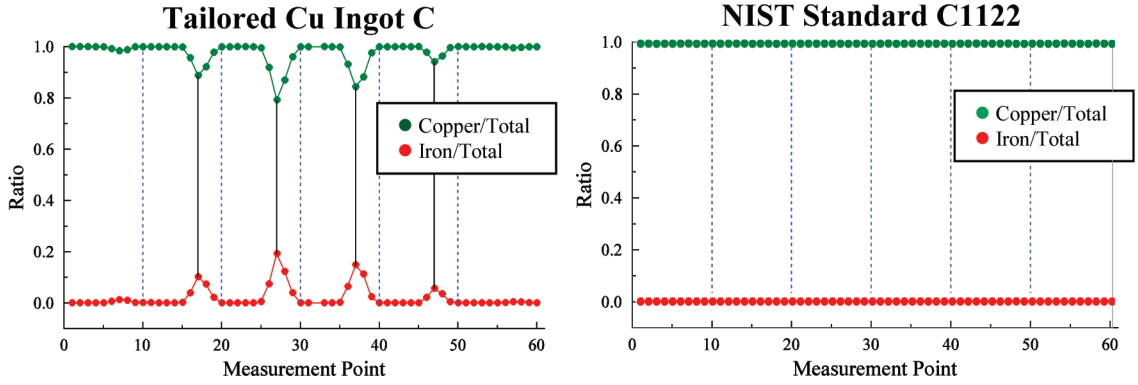

Figure 10. (Left) Ratio of XRF photon counts to total spectrum counts for Cu (green points) and for Fe (red points), compiled from data of Figure 8 for a magnetic spot on Ingot C. Each pair of points (green and red) represents a single spectrum from a point on the scanning grid of Figure 9a. In strongly coordinated fashion, near four grid vertex points (no. 17, 27, 37, and 47) the Cu emission drops while the corresponding Fe emission climbs. (Right) Analogous data for Cu (green points) and Fe (red points) from a NIST C1122 standard sample. All ARTAX analysis parameters were identical for runs with ingot C and the NIST standard: W tube, 650 μm collimator, 40 kV, 1000 μA, 315 μm Al Filter, 40 s/point scans.

counts for the Cu K_α emissions with those for SFe, recorded throughout the scanning grid, as shown in Figure 13b. Again, this plot exhibits an approximately quantitative and remarkably strong inverse correlation between the Cu and SFe emissions.

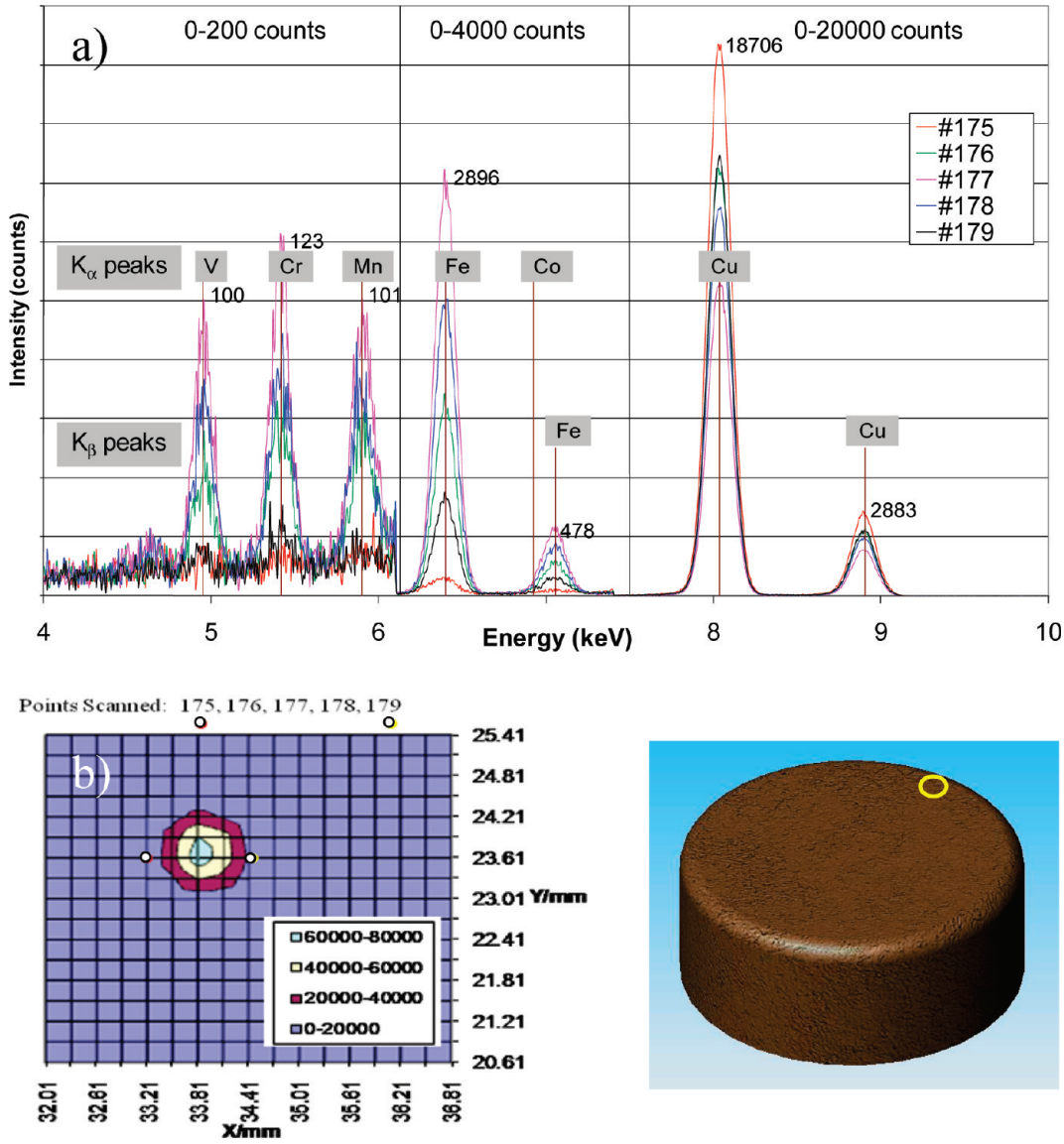

Figure 11. (a) XRF spectra for ingot C for a magnetically active spot located (upper right, yellow circle) near the edge of the bottom of the ingot. (b) Grid pattern in format like Figure 8; white dots mark start (no. 175) and end (no. 179) of grid positions for the five spectra scans (color-coded). For each element, the ordinate scale has been normalized to the intensity observed at no. 177, in order to exhibit most clearly that the Cu K_α and K_β intensities vary the same way but opposite to the SE intensities. Raw pulse counts are shown for grid position no. 177. ARTAX parameters are the same as in Figure 8.

There is extensive and accurate information about attenuation of XRF spectra by thin metal filters, which influence both the penetration depth of the bombarding X-rays and escape of the fluorescence photons. As described in Appendix B, those data indicate that a thickness of about 10 μm of Fe, located within 60 μm of the surface, would be required to reduce the Cu K_α emission by 90%. This is an extremely severe requirement. Such a high concentration of iron in the magnetic spots would be clearly visible to the naked eye, but in fact the spots are not visible. Moreover, if filtering is involved, the inverse correlation between Cu and Fe emissions should be an exponential rather than linear relation. The GD-MS analysis, as seen in Figure 4, confirms that the impurity Fe content of samples from the interior of our copper ingots, tailored or not, is only a few ppm. Thus, an extremely efficient agglomeration process would be required to create local concentrations of Fe several orders of magnitude higher in the magnetic spots as needed to appreciably attenuate XRF from copper.

Other phenomena familiar in XRF spectroscopy also appear untenable as explanations of the observed drastic attenuation of Cu emission. To attain a 90% attenuation by simply diluting copper with iron in the magnetic spots would require even more Fe than the filtering process. Secondary processes, in which a fluorescence photon from Cu ejects a K-shell electron from Fe would induce attenuation of the Cu signal accompanied by enhanced Fe fluorescence. Such effects, however, are ordinarily insignificant and would require a much greater Fe concentration to become a major factor.

Conclusions

The experimental results described here have many surprising aspects. We know of no previous observation of thermal operations on copper that induce magnetic spots. Probing with XRF the elemental composition of those spots, as well as that for samples from the interior of tailored ingots, has revealed very unusual features that invite the designation of *sensitized elements*. At present, this is merely a convenient shorthand term. It simply indicates that for those elements, XRF emissions appear with intensity far higher than would be expected from

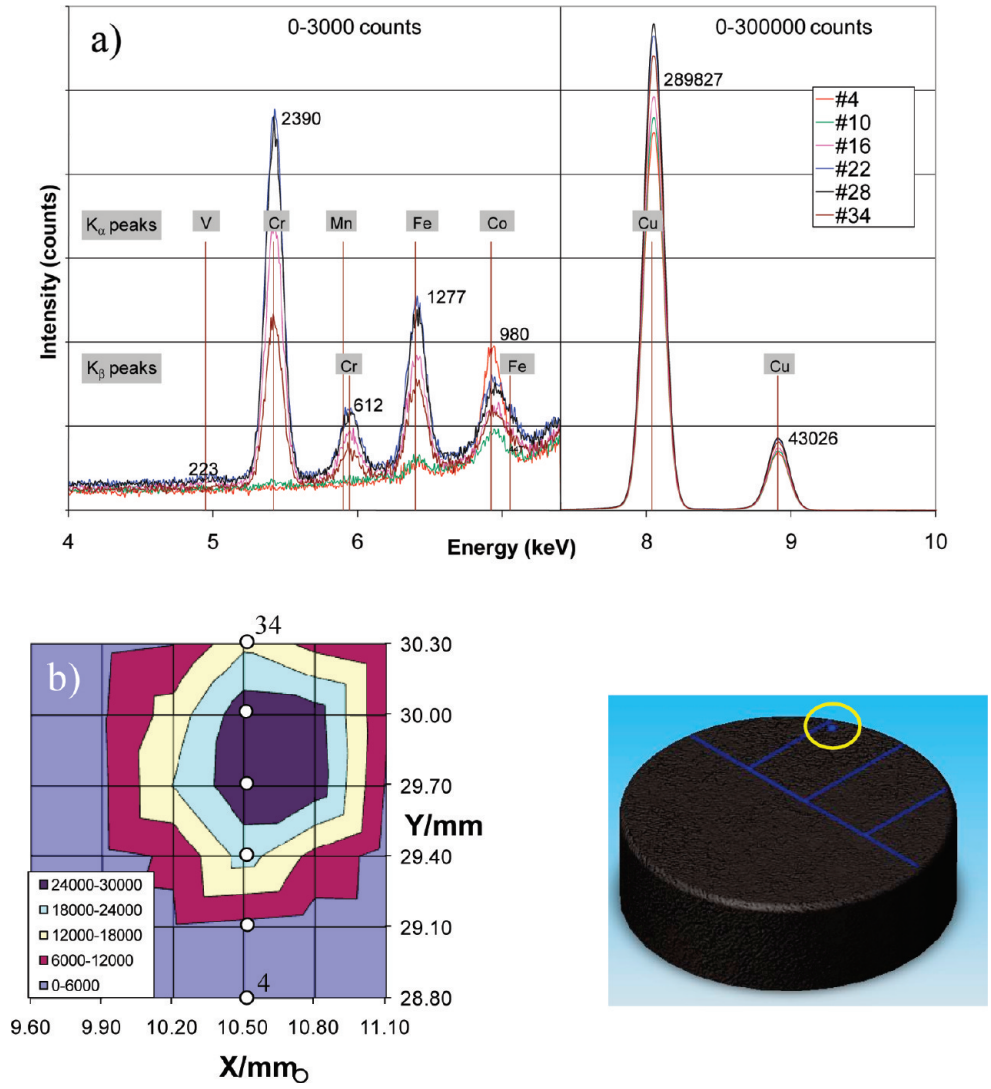

Figure 12. XRF spectra for copper ingot D (14-08-04) for a magnetically active spot located (as pictured at upper center, yellow circle) near the edge of the ingot bottom. (b) Plot showing Fe K_α signal pulses detected across grid pattern for scanning over spot area. White dots mark grid positions for six spectra scans: start (no. 4) and end (no. 34). ARTAX parameters same as in Figure 7 except used 600 s/point scans.

the amount present of that element, as determined by other reliable analytical means.

We have relied chiefly (but not solely) on high-resolution GD-MS (lower detection limit typically <0.05 ppm, much lower than for XRF) to monitor elemental composition of the bulk copper samples. Multiple GD-MS analyses were obtained for raw "chop" material, melted raw materials (in graphite, alumina, and zirconia crucibles) and tailored samples. All these analyses (e.g., Figure 3) show no appreciable differences between the untreated starting and tailored copper samples. Moreover, XRF elemental analysis agrees (within its sensitivity) with the GD-MS results for untreated starting materials, as well as for a "blank" ingot that had been melted and held in the reactor for the same total time but not subjected to the thermal cycling used in tailoring runs.

The thermal cycling involved in tailoring appears to somehow markedly enhance XRF emissions from SEs. Our experimental results pertaining to magnetic spots on copper are in accord with, but more striking than, evidence for SEs found previously in our laboratory for other tailored materials, including aluminum, iron, cobalt, and silicon. The most startling aspect of the XRF from the spots is the drastic attenuation of Cu emissions, inversely correlated with SE emissions.

The interpretation of the origin of SEs remains problematic. At present, we consider the most telling aspect is that for tailored samples, from ingot interiors rather than the surface, the ARL XRF spectra indicate much larger amounts of the putative SEs than the impurity content determined by GD-MS. This suggests that tailoring may strongly enhance the transition probabilities for emissions from the impurities (by amplifying X-ray ejection of K-shell electrons or the fluorescent refilling or both). If so, (e.g., much less Fe might produce filtering and attenuation of Cu emissions than would be required for untailored samples), a possibly important role of tailoring may be to foster chemical interactions of impurities with copper. It is unclear how much that might affect XRF enhancement and other SE properties. However, e.g., copper could become directly involved in magnetic spots if such interactions introduce cupric ions, which have a $(3d)^9$ valence electron configuration.

In current work, we find further unusual behavior of SEs. This includes details of temporal variations that can now be examined because the new XRF tools enable us to track SEs in real time. Also, we have found that SEs often are hypersensitive to sequenced irradiation by light that in untailored material has no effect. We hope that theory will be forthcoming to elucidate such experimental results.

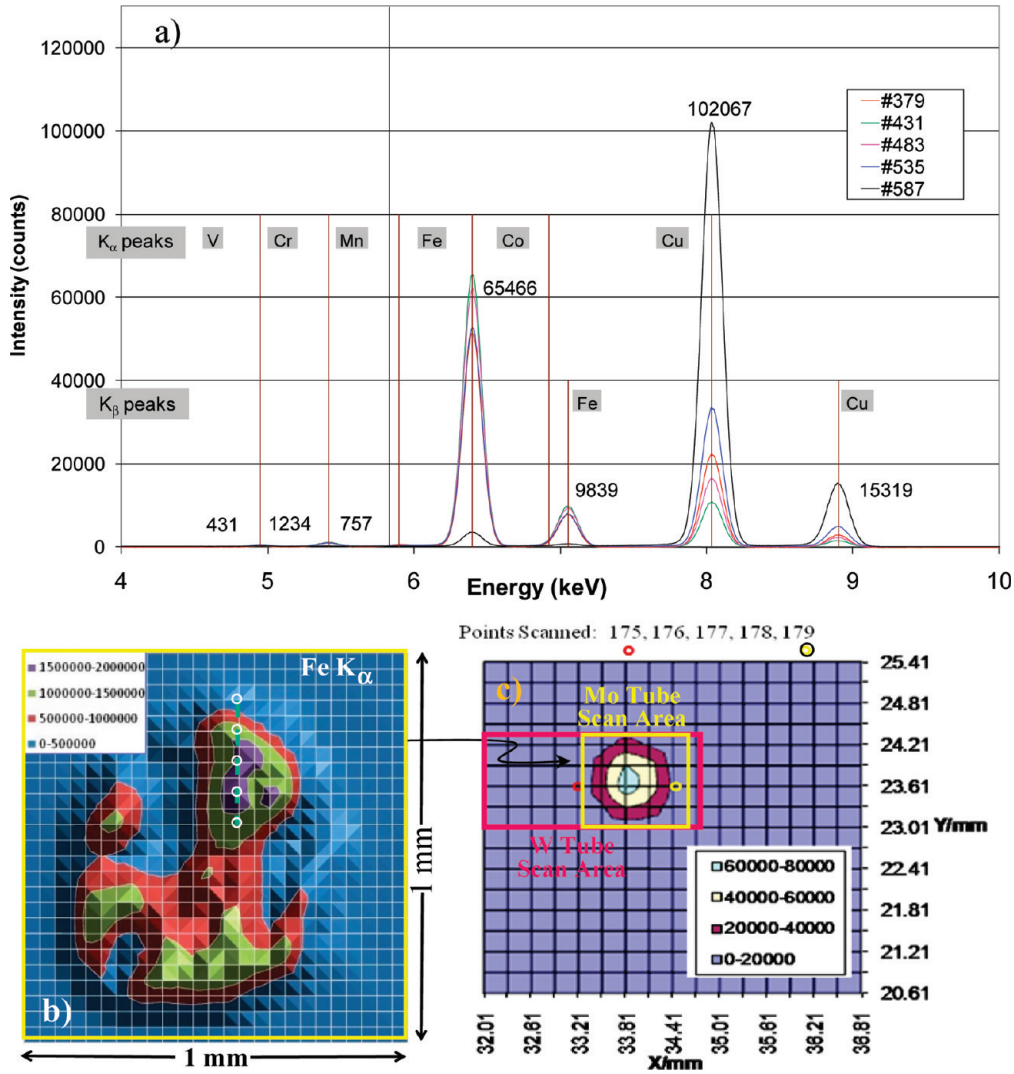

Figure 13. (a) ARTAX ED-XRF spectra of five measurements (no. 379, 431, 483, 535, and 587) taken from the same magnetically active spot on ingot C as shown in Figures 9−11 but obtained using a Mo excitation tube, with parameters 40 kV, 700 μA, 315 μm Al filter, 60 μm polycapillary lens (~70 μm observation region), 120 s scan/spot, 50% overlap. Note here that the ordinate scale displays the raw pulse counts so that the relative intensities of emissions from different species can be compared directly. (b) Scanning grid pattern akin to that shown in Figure 11 showing higher resolution obtained with Mo vs W tube. Spectra were obtained at points marked by aqua lines/white circles along the vertical path indicated. (c) Overlay of Mo scanned area (shown in green) on the spectral surface map obtained using the W tube (cf. Figure 11).

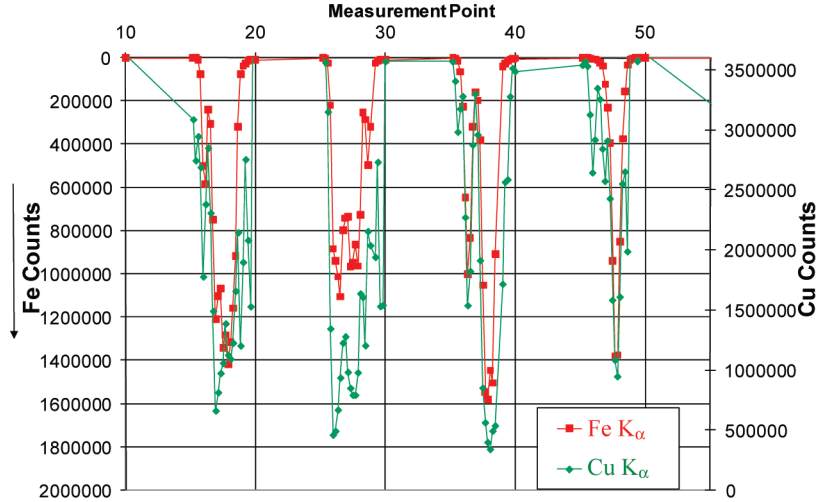

Figure 14. ARTAX ED-XRF pulse counts for Cu K_α emissions (green) and corresponding SFe K_α emissions (red). Each pair of points represents a single spectrum like those shown in Figure 13, recorded at successive positions along four paths on the scanning grid (cf. Figure 10). The data shown are raw pulse counts. To allow direct comparison, the Fe concentrations have been plotted downward (inverse scale). Note the left and right ordinate scales are not identical. The Cu emissions drop (near scanning points no. 16, 27, 38, and 48) by as much as 90% whereas the SFe emissions climb in an approximately converse pattern.

Acknowledgment. This work was made possible through the extensive support and continuous advice of John Preston, the fortitude and astute contributions of Claire Chanenchuk, and the generous sharing of his immense XRF expertise by Bruce Kaiser. We are grateful as well for the unstinting efforts of Bob Braunsdorf, Chris Brodeur, Chris Heleen, Steve Lemoi, Tom Preston, Jon Welch, and other staff members, as well as the owners and advisors of Continuum Energy Technologies.

Appendix A.

Bragg Scattering. The three standard steps in testing for Bragg scattering in XRF consist of (1) identifying energies of expected diffraction peaks and examining whether (2) changing angles of incidence on the sample shifts location of peaks or (3) a suspected Bragg peak disappears when a filter is installed to block the incident beam energy required to produce that peak.

(1) An X-ray diffraction analysis of tailored Cu samples was performed by Evans Analytical Group (Round Rock, TX). This provided *d*-spacings, from which the energies corresponding to Bragg peaks were calculated that pertain to the Bruker ARTAX geometry (fixed tube angle of 54.07°, incident beam detector angle 125.93°). Only one of the emissions in the XRF spectra of Figures 7−11 is a candidate Bragg peak (6.39 keV at Cu *hkl* 311).

(2) XRF spectra for our tailored copper ingot C were taken for five different angles of incidence (0°, 3°, 5°, 10°, and 20°). Over the entire range of angles, the observed peaks did not appear to shift to higher or lower energies, whereas substantial shifts should occur for features resulting from Bragg scattering.

(3) The candidate Bragg peak at 6.39 keV noted above is of special interest, as it would occur very close to the XRF from the Fe K_α emission at 6.4 keV. We used a 315 μm Al filter to "harden" the incident X-ray beam by removing energies below ~8 keV, which eliminates Bragg scattering in that range. This was found not to appreciably alter the observed XRF spectra; no peak shifts occurred in the region of interest, 5−8 keV.

For details pertaining to these tests for Bragg scattering, see the online technical bulletin.[9]

Appendix B.

Estimates of Iron Filtering or Aggregation. As seen in Figures 8−14, in XRF of magnetic spots on tailored copper the emissions from Cu are strongly attenuated and inversely correlated with those from SFe and other SEs. This prompts estimates of whether enough impurity Fe could possibly aggregate in the spots to account for the observed attenuation, without invoking any enhancement in the intensity of XRF lines from SEs.

As use of thin metal filters to attenuate XRF is standard practice, values of the mass attenuation coefficients, μ_m, are available for Fe and other metals as functions of the X-ray energy.[10] These govern the exponential reduction of transmission via Beer's law, $I = I_0 \exp(-\mu_m x \rho)$, with I_0 the initial intensity, I that transmitted, x the path length, and ρ the density of the filtering material. For iron, $\mu_m = 304.8$ and 236.3 cm^2/g, respectively, at 8.05 and 8.90 keV, the energies of the Cu Kα and K_β fluorescence lines, and $\rho = 7.86$ g/cm^3. An online technical bulletin[9] includes graphs and tables, computed by Jon Welch, that display the percent attenuation of Cu K_α and K_β X-rays, and others of various energy, as functions of the thickness of an iron layer covering the copper surface. For instance, for 30% attenuation of the K_α line the thickness of the iron layer needs to be 1.4 μm; for 90% attenuation about 9.3 μm. If located in a spot of area 4 mm^2, the corresponding amounts of Fe would be 0.05 mg and 0.3 mg, respectively. Those amounts are large enough to be visible to a naked eye, which is not so for the actual magnetic spots. For Fe dissolved in the copper (within 60 μm below the surface, escape zone for the Cu K_α and K_β lines) rather than in a layer, its amount would have to be larger to produce the same attenuation of the Cu emissions.

The online technical bulletin[9] also includes calculations examining models for transport of iron impurities, either existing in the copper ingot prior to tailoring or introduced during it from the refractory crucible, to agglomerate into spots on the ingot surface. GD-MS, recording mass spectra produced by gas discharge ionization, is highly reliable for bulk elemental analysis. It was conducted on a wide range of copper samples. These included material taken from interior, as well as surfaces of ingots, both before and after the tailoring operations, and processed in different crucibles (of graphite, zirconia, or alumina). All showed essentially the same impurity levels (with lower detection limit typically ≤0.05 ppm). The average Fe concentration of untreated and tailored copper was 3.5 ppm, with a variation of ±3 ppm. Solute distribution as liquid metals undergo solidification has been extensively studied.[11] If only a few ppm of Fe exist in the bulk ingot, however, model transport calculations[9] find this is much too low to agglomerate the Fe into small surface spots at levels required to produce substantial attenuation of Cu emissions.

Contamination transferred from the refractory crucible to the molten copper or deposited on the surface of the ingot during solidification is a more plausible prospect. Occasional specks were observed on ingots that obviously came from the crucible or its lid, when not brushed away, these can affect ARTAX spectra, as noted in Figure 9. The crucibles whether chiefly made of graphite, alumina, or zirconia contain Fe_2O_3 but in varying amounts; GD-MS analysis finds the average Fe content ~4, 200, and 500 ppm, respectively. At the high temperature used in tailoring (>1300 °C), copper can reduce Fe_2O_3 to Fe_3O_4. The latter is magnetic but undergoes air oxidation back to nonmagnetic Fe_2O_3, which might account in part for the decay of magnetism in some of the observed spots. Yet, as noted above, the GD-MS analysis of ingots does not indicate any significant differences in the elemental composition of copper ingots whether subject to the tailoring procedure or not. In view of the wide variation in Fe content between the crucibles, it is particularly significant that GD-MS did not find any corresponding change in Fe content for ingots processed using graphite, alumina, or zirconia crucibles. The tailored ingots, regardless of crucible or protocol used, contained the same amount of Fe as the starting material (copper chop with 3−5 ppm Fe). Moreover, in "blank" runs, molten copper ingots that did not undergo tailoring but were held in crucibles for the same period of time did not develop magnetic spots and in XRF spectra of those ingots sensitized elements did not appear.

References and Notes

(1) Nagel, C. J. , "Composition of Matter Tailoring: System I", No 6,572,792, issued June, 2003.

(2) Nagel, C. J., "Composition of Matter Tailoring: System I CIP", No 6,921,497, issued July, 2005.

(3) The tailoring procedures of Figure 1 employ some thermal sweeps symmetric in time, others asymmetric. Temperature changes incurred for copper range, with few exceptions, between ±5 and ±40 °F over an approximate time span of 15 min. In the "simplest" version used here, the temperature fluctuations were small and rapid about ±5 °F in 1−2 min and asymmetric in both temperature and time.

(4) A 650 μm collimator was used with the W tube for excitation, and a 60 μm microfocus lens was used for the Mo excitation tube, resulting in an average size of observation region of 65−70 μm.

(5) Scofield, J. H. *Phys. Rev. A.* **1974**, *9*, 1041.

(6) Han, I.; Sahin, M.; Demir, L.; Sahin, Y. *App. Rad. Iso.* **2007**, *65*, 669.

(7) Private communication from Bruce Kaiser. The peak area ratio of Fe K_α/K_β is 5.60 for pure iron and ranges from 5.72 to 6.30 as measured from XRF spectra obtained using Bruker TRACER III operating at 40 kV and 1.5 μA with a composite 12 mil aluminum, 1 mil titanium filter. This range includes analysis of numerous alloys, e.g., Mn increases the apparent Fe K_α peak (6.40 keV) by virtue of an underlying Mn K_β (6.49 keV), while simultaneously suppressing the Fe K_β peak (7.06 keV) as its emissions excite the K absorption edge of Mn (6.54 keV). Likewise, if Cr is present, its K absorption edge (5.99 keV) can be excited by Fe K_α emission, thereby decreasing the apparent Fe K_α peak. Such effects must be taken into account to arrive at the true Fe K_α/K_β ratio.

(8) The mode of plotting data used in Figure 10 is designed to exhibit clearly the locations of any correlated changes in the Cu and Fe emissions. However, it hides information about the magnitudes of the emissions. The Cu photon counts are roughly 10-fold larger than those for Fe.

(9) http://www.cenergytech.com/technology.htm.

(10) http://physics.nist.gov/PhysRefData/XrayMassCoef/ElemTab/z26.html.

(11) Flemings M. C. *Solidification Processing*; McGraw-Hill: New York, 1974.

JP908299Q